Fuel Processing Technology 253 (2024) 108028

Contents lists available at ScienceDirect

Fuel Processing Technology

journal homepage: www.elsevier.com/locate/fuproc

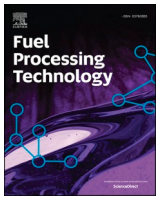

Sustainable carbon-based nickel catalysts for the steam reforming of model compounds of pyrolysis liquids

Paula Cabrera-Reyes, José Palomo, Francisco J. García-Mateos, Ramiro Ruiz-Rosas *, Juana M. Rosas, José Rodríguez-Mirasol, Tomás Cordero

Universidad de Málaga, Andalucia Tech., Departamento de Ingeniería química, Campus de Teatinos s/n, 29010 Málaga, Spain

ARTICLE INFO

Keywords:
Hydrogen
Activated carbon
Ni catalyst
Steam reforming
Pyrolysis liquids
Biomass waste valorization

ABSTRACT

Steam reforming of biomass-derived pyrolysis liquids (bio-oil) to produce hydrogen with carbon-based Ni catalysts is gaining attention due to their advantages in terms of cost, sustainability and activity. However, the catalytic activity at long times on stream is compromised by either coke deposition or gasification of the support. To face these drawbacks, two activated carbons have been studied as Ni catalyst support: a microporous carbon of high purity and a mesoporous carbon with phosphorus surface groups. The activity and long-term stability of these catalysts have been studied for the steam reforming of model compounds of bio-oil. The microporous support provided a slightly higher H_2 production and lower contribution of methanation reaction. However, gasification of this support after 20 h led to a decline in the activity, and massive formation of carbon nanotubes and coke. Nevertheless, the resulting material maintained an outstanding stability with high and stable H_2/CO ratio for 50 h. The P-containing catalyst showed a remarkable long-term stability, but lower H_2/CO ratio. Carbon gasification was less significant in this catalyst due to the presence of surface phosphorus groups, and the generation of nickel phosphides, which hampers the growth of pyrolytic carbon and carbon nanotubes, leading to a superior stability.

1. Introduction

In the current global energy scenario, fossil fuels still represent the main source for obtaining primary energy [1]. However, the depletion of these natural resources, together with the increasing concerns about climate change, are setting new directives and plans towards the decarbonization of energy by using hydrogen as alternative fuel [2]. Hydrogen is, indeed, considered nowadays as an ideal energy carrier and a fundamental building-block for the petrochemical and metallurgical industries. The production of hydrogen is mostly accomplished via catalytic steam reforming of natural gas and naphtha [3]. However, if a reduction in the reliance on fossil fuels is targeted, alternative and sustainable feedstocks and routes to produce hydrogen are required.

In this context, lignocellulosic biomass constitutes a promising sustainable feedstock for energy applications due to its great availability and low price [4,5]. In addition, if lignocellulosic materials, such as wood, pruning leftovers or other agroforestry wastes, are used for such energetic purposes, no competition with food crops will take place [6]. The production of hydrogen from biomass can be achieved through pyrolysis, which generates a solid, a liquid and gas fraction. The gas fraction is usually rich in CO_2 and methane, which can be upgraded to hydrogen through steam or dry reforming [7,8]. The yield of the liquid fraction (bio-oil) can be considerably increased under fast or flash operating conditions [9]. The aqueous fraction of bio-oil can be upgraded or used to obtain hydrogen by catalytic steam reforming [10–12].

Several catalysts have been investigated for hydrogen production by bio-oil steam reforming. Although noble metals, such as Rh, Pt, or Ir, have demonstrated a fairly good catalytic performance [13], the high cost of these elements somehow hinders their use in industrial applications [14]. On the other hand, transition metals, including Co, Ni and Fe, have been also analyzed as potential catalysts. Within these alternative active metals, Ni-based catalysts have received a great deal of attention due to its high activity and relatively low cost [15]. Different elements as Cu, Mg or La have been identified as suitable promoters [16,17], although they would increase costs and require additional preparation steps. As for the catalyst support, different inorganic oxides, such as

* Corresponding author.
E-mail addresses: paulacabrera@uma.es (P. Cabrera-Reyes), palomo@uma.es (J. Palomo), garciamateos@uma.es (F.J. García-Mateos), ramiro@uma.es (R. Ruiz-Rosas), jmrosas@uma.es (J.M. Rosas), mirasol@uma.es (J. Rodríguez-Mirasol), cordero@uma.es (T. Cordero).

https://doi.org/10.1016/j.fuproc.2023.108028
Received 29 October 2023; Received in revised form 19 December 2023; Accepted 23 December 2023
Available online 3 January 2024
0378-3820/© 2023 Published by Elsevier B.V. This is an open access article under the CC BY-NC-ND license (http://creativecommons.org/licenses/by-nc-nd/4.0/).

ZrO_2 [18], dolomite [19], Al_2O_3 [20] or aluminum oxide spinel [21] have been investigated. Amongst them, alumina supported catalysts have been extensively studied due to its high mechanical and thermal stability and high surface area [10]. However, the use of this support presents some drawbacks, such as its low hydrothermal stability [22] and the need of high reforming temperatures (ca. 750 °C) to achieve stable operation [23]. Furthermore, the surface acidity of alumina has been reported to promote undesired polymerization reactions, giving rise to additional problems related to catalyst deactivation by coke deposition [24]. Alternative catalysts, as coal fly ash, have been proposed to increase industrial competitiveness of steam reforming processes, at the cost of using a fossil-derived product of low sustainability [25]. The role of catalytic supports and promoters in the steam reforming reaction has been studied in the literature. For instance, Garcia et al. analyzed the activity of catalysts as a function of their composition, finding a strong impact of Mg and La as promoters [14], while Furusawa et al. reported an improved catalytic activity of Al_2O_3 as support over ZrO_2, MgO, CeO_2 and TiO_2 [26]. The support also modifies the nature of coke formed on the process, as stated by He et al., who reported an increased formation of active CNTs at low S/C ratios for γ-Al_2O_3 over α-Al_2O_3 Ni-catalysts in the SR of toluene [27].

It is also worth to mention, that conventional inorganic supports require, in some cases, energy intensive preparation methods, such as hydrothermal synthesis, that make resulting catalyst costly. Besides, once these catalysts are irreversibly deactivated the recovery of the active metal phases constitutes a challenge. In this context, the use of activated carbons as alternative supports for Ni-based steam reforming catalysts would present interesting techno economical as well as environmental advantages. These materials present outstanding physicochemical properties, such as high specific surface area, good thermal conductivity, and high thermal and chemical stability [28]. Another remarkable feature activated carbon possesses is the possibility of tuning its surface chemistry through the incorporation of different heteroatoms on its surface [29–32]. Besides, these carbon-supports can be prepared using industrial waste as carbon precursor, reducing the cost of the catalyst and the carbon footprint. Furthermore, the use of these catalysts could be very interesting from the perspective of increasing the process circularity and sustainability. In the event of irreversible catalyst deactivation, the recovery of the active phase can be accomplished by gasification or combustion of the carbon support, obtaining energy and a solid residue (i.e., ashes) that mostly contains the metal catalyst phase.

Some recent studies on the use of carbon support for catalytic steam reforming can be found in literature [33–36]. In this line, Yahya et al. used activated carbon-supported Ni—Co catalysts for hydrogen production from toluene steam reforming [36]. Di Stasi et al. reported the use of Ni—Co catalysts supported on physically activated straw-derived biochars for different bio-oil model compounds steam reforming [35]. Partial deactivation with time-on-stream was observed for these carbon-based catalysts under certain operation conditions due to the adsorption of heavy compounds on the active sites of the catalyst.

The main drawback of carbon-based catalytic systems for SR of pyrolysis liquids lies on their low gasification resistance. In order to avoid deactivation via coke deposition, Ni-based SR catalysts are operated at high steam-to-carbon (S/C) ratios and temperatures [37], which not only hampers the energy balance of the process, but also leads to the gasification of the carbon supports by the excess of steam in the gas stream. The use of conventional alkaline and alkaline earth promoters (efficient carbonaceous gasification catalysts) [38] to enable the catalytic SR operation under softer conditions would only aggravate the gasification of the carbon supports, while the addition of other promoters as rare earths [39] or noble metals [20] would severely hinder the sustainability of using biomass-derived carbon supports. However, other non-expensive heteroatoms could serve as catalytic promoters for carbon supports. In this sense, Lu et al. studied tar model compounds for steam reforming using char-supported nickel catalysts [40]. The authors found that the addition of P into the catalyst resulted in a better catalytic performance, which was attributed to the presence of acid sites together with an enhancement in the Ni dispersion. This interesting effect of P on the enhanced catalytic stability of Ni-based catalysts by reducing coke deposition has been also reported for other inorganic catalysts [41].

Cordero et al. have reported several works on the preparation of activated carbons by chemical activation of different lignocellulosic waste with phosphoric acid [42,43]. The use of this chemical as activating reagent, under particular temperature and impregnation ratio conditions, yields mesoporous carbon materials presenting phosphorus surface complexes, mainly in the form of C-PO_3 and C-O-PO_3 groups, exhibiting a high thermal and chemical stability, remaining on the carbon surface after the washing step [44]. These phosphorus complexes provide the activated carbons with surface acidity and a high oxidation resistance, making them outstanding candidates for catalysis applications [45–47].

In the present work, the steam reforming of bio-oil model compounds for the sustainable hydrogen production using Ni-loaded biomass-derived activated carbon catalysts was studied. The preparation conditions of these ACs were carefully selected not only to achieve a high specific surface area to improve the dispersion of the active phase, but also to obtain i) a microporous support of high purity ii) a mesoporous support with phosphorus surface groups. For this purpose, the activated carbons were prepared via partial gasification of a biochar derived from a lignocellulosic waste, pistachio shell, with CO_2 activation and by chemical activation of the same biomass waste with phosphoric acid. The key role of porosity and phosphorus surface groups in the resulting catalysts was in-detail analyzed. The stability with time on stream of the resulting catalyst was also assessed.

2. Material & methods

2.1. Preparation of catalysts

Pistachio shells were selected as raw material to prepare the activated carbons used as catalyst supports. The as received pistachio shell (referred as PS) was washed with deionized water at room temperature, dried and grinded and sieved to particle sizes lower than 2 mm. For the preparation of the chemically activated carbon, PS was impregnated at room temperature with aqueous phosphoric acid (85% *w*/w) using an acid/PS impregnation mass ratio of 3:1. After that, the impregnated sample was dried for 24 h at 60 °C in an oven. This mixture was subsequently activated at 500 °C in a horizontal tubular furnace (heating rate of 10 °C/min) in a N_2 atmosphere (99.999%, 150 mL/min STP) for 2 h. Previous studies of our research group [42,48] concluded that activation temperature of 500 °C and H_3PO_4 impregnation rate of 3 are adequate to obtain an activated carbon with high carbon preparation yields and high development of the apparent surface area and mesopore volume.

The activated samples were washed with distilled water at 60 °C until neutral pH. The resulting activated carbon, PSP, were dried at 120 °C for 24 h and weighted for the determination of the preparation yield. Afterwards, they were grinded and sieved between 50 and 100 μm. A phosphorus-free activated carbon was prepared by partial gasification with CO_2. PS was firstly carbonized at 800 °C in a conventional tubular furnace under N_2 atmosphere (150 mL/min STP) with a heating rate of 10 °C/min and a holding time of 2 h. Then, a partial gasification of the resulting sample was carried out at the same temperature under CO_2 atmosphere for 2 h (burn-off: 55%), obtaining PSG activated carbon. These preparations conditions were chosen in order to obtain a similar apparent surface area in both PSP and PSG carbons.

The loading of the active phase on both supports was carried out by incipient wetness impregnation method. A calculated amount of nickel precursor ($Ni(NO_3)_2{\cdot}6H_2O$, VWR lab) was added in order to reach a nominal 10% Ni mass loading on the final carbon-based catalyst system. The impregnated carbons were dried overnight in an oven at 120 °C, followed by a thermal treatment under inert atmosphere (N_2, 150 mL/

min STP, heating rate of 10 °C/min) at 700 °C for 4 h, in order to decompose the nickel salt and promote the formation of the active phase. The final obtained catalysts were denoted as PSP-Ni for the P-containing, H_3PO_4-activated carbon, and PSG-Ni for the P-free, physically activated carbon.

2.2. Characterization of catalysts

The porosity of the prepared catalysts (before and after reaction) was characterized by N_2 adsorption–desorption at −196 °C and by CO_2 adsorption at 0 °C (ASAP 2020, Micromeritics Instruments Corp., Norcross, GA, USA). The samples were outgassed for at least 8 h at 150 °C under vacuum prior to the analysis.

From the N_2 isotherm data, the apparent surface area (A_{BET}) was calculated from the Brunauer−Emmett−Teller equation (BET). The P/P_0 range was selected in accordance to Rouquerol's criteria [36]. The α-s method was used to obtain the values of micropore volume (V_s). The difference between the maximum volume adsorbed (V_{tot}) at a relative pressure of 0.96 and the micropore volume (V_s) determined the value of the mesopore volume (V_{mes}). From the CO_2 isotherm data, the Dubinin−Radushkevich equation was applied to calculate the narrow micropore volume (V_{DR}) [36].

The surface chemistry of the fresh and used catalysts was studied by X-ray photoelectron spectroscopy (XPS), which was carried out in a spectrophotometer 5700C (Physical Electronics)/PHI 5000 VersaProbe II (Physical Electronics, Chanhassen, MN, USA), with MgKα radiation (1253.6 eV). For the analysis of the XPS peaks, the maximum of the C1s peak was set at 284.5 eV and used as a reference for the other peaks.

X-ray diffraction patterns (XRD) of the samples were recorded in the region 2θ = 5–90° on an EMPYREAN diffractometer of PANalytical using CuKα monochromatic radiation (operation value 45 kV and 40 mA), a PIXcel detector and Soller slits (incident and diffracted beam) of 0.04 rad. The average crystallite sizes (D_p) were estimated by the application of the Scherrer equation (Eq. (1)) from the X-ray wavelength (λ) and the position and full width at half maximum (FWHM) of the peaks:

$$Dp = \frac{0.94 \cdot \lambda}{FWHM \cdot cos\theta} \tag{1}$$

Temperature programmed reduction with hydrogen (H_2-TPR) was also used to study the reducibility of the metallic species on the surface of the activated carbons. In these experiments, 50 mg of sample were loaded in a quartz fixed-bed microreactor, placed inside a vertical furnace with temperature control, and heated up to 120 °C in a 5% (*v*/v) H_2 in Ar stream (100 mL/min). H_2 consumption and CH_4, H_2O, CO, and CO_2 generation were monitored by mass spectrometry (Pfeifer Omnistar GCD-301), recording the signals m/z = 2, 15, 18, 28 and 44, respectively. Signal m/z = 32 was also recorded in order to ensure the absence of oxygen in the experiment, while m/z = 40, associated to the argon carrier, was followed for reference purposes.

Raman spectra were recorded with a micro-Raman system (Renishaw) using an Ar + laser at 514 nm as the excitation source, with a spectral resolution of 2 cm. Two scans were carried out using a power of 0.27 mW, 10 s of acquisition time and a 50× magnification.

The morphology of the catalysts was studied by transmission electron microscopy (TEM) in a FEI Talos F200X microscope at an accelerating voltage of 200 kV and in a high annular dark field (HAADF). Energy dispersive X-ray (EDX) mapping analysis of the samples gave information about their chemical composition and the distribution of carbon, oxygen, phosphorus and nickel.

2.3. Steam reforming reaction experiments

Steam reforming experiments were carried out at atmospheric pressure in a fixed-bed microreactor (i.d. 4 mm) placed inside a vertical furnace with temperature control. An equimolar mix of acetone, ethanol and acetic acid (0.75% *v*/v each) was used as model compound to simulate the ethanol extract of pistachio shell bio-oil. The steam reforming of each one of these compounds would proceed in accordance with the next set of reactions:

$$C_nH_mO_k + (2n-k)H_2O \rightarrow n\,CO_2 + \left(2n-k+\frac{m}{2}\right)H_2 \tag{2}$$

The steam reforming reaction of every oxygenated compound is described by Eq. (2) and therefore was taken into consideration to define the global stoichiometry of the process.

The steam to carbon molar ratio (S/C) was set to the stoichiometric value in order to minimize the steam gasification of the carbon support. The water and the compounds simulating the bio-oil were fed together to the system with a 1.357 mL/h rate by using a syringe pump (Cole-Parmer® 74,900–00-05 model) with argon (purity of 99.999%, Linde, 180 mL/min STP) as carrier gas, achieving a total flow rate of 200 mL/min STP. A scheme of the experimental set-up can be shown in Fig. S1.

To avoid condensation of any compound, all pipelines were heated up to 120 °C.

In a typical experiment, 50 mg of catalyst (space time of 50 g_{cat}·s/mmol) were loaded in a quartz reactor (inner diameter: 4 mm) The catalyst bed was placed in the isothermal zone of the reactor, and an internal thermocouple was used to ensure that the temperature of the bed is kept constant. The reaction took place under isothermal conditions at 600 °C or 700 °C. Before starting the reaction, a reduction stage consisting of a treatment of the catalysts at 600 °C with a 20% H_2 in Ar stream for 2 h, was carried out in some of the experiments. An experiment with only water as reactant in the gas inlet was also carried out for each catalyst to evaluate the possible gasification of the activated carbons under the reaction conditions.

Concentrations of gas reactants and products were measured by an online Varian CP-4900 gas micro chromatograph (Agilent), equipped with capillary columns: 5 Å molecular sieve, PPQ, and wax columns. The mass variation of the catalytic bed was quantified by directly weighing the reactor before and after reaction.

The conversion for each reactant was defined based on the inlet and outlet concentration (Eq. (3)), whereas the yield of the products of interest was calculated from the corresponding product outlet concentration with respect to the stoichiometric concentration of hydrogen or carbon. According to this, the conversion of reactant and the yields of H_2 (Eq. (4)) and the carbon-containing by-products (Eq. (5)) were defined as follows:

$$X_i = \frac{C_{i,in} - C_{i,out}}{C_{i,in}} \tag{3}$$

$$Y_{H_2} = \frac{C_{H_2,out}}{C_{H_2O,in} + 3 \cdot C_{CH_3CH_2OH} + 3 \cdot C_{CH_3COCH_3} + 2 \cdot C_{CH_3COOH}} \tag{4}$$

$$Y_p = \frac{m_p \cdot C_p}{\sum (m_i \cdot C_{i,out})} \tag{5}$$

where X_i represents the conversion of each reactant, Y_{H2} the yield of hydrogen, and Y_p the yield of each carbon-containing product. $C_{i,in}$ and $C_{i,out}$ are the inlet and outlet concentration of corresponding *i* molecule, respectively; and, finally, n_i and m_i stands for the total number of H or C atoms in every reactant, respectively.

Conversion and yield values at equilibrium have been estimated by simulating the steam reforming reaction with Aspen HYSYS V10 simulation software. A Peng-Robinson thermodynamic package together with all the detected compounds were used as input. The inlet was fed to an isotherm Gibbs reactor module, where working conditions and all the possible reactions were set, and which provides both composition of the gaseous outlet and amount of generated coke by minimizing the Gibbs free energy of the reaction system.

3. Results and discussion

3.1. Characterization of the catalysts

The N_2 adsorption-desorption isotherms at −196 °C of the physically activated pistachio shell (PSG) and chemically activated pistachio shell (PSP) are compared in Fig. 1. Notable differences can be appreciated in the nitrogen uptake and shape of the adsorption isotherms. PSG shows a type I adsorption isotherm according to the IUPAC classification [49], indicative of the presence of mainly a microporous structure, while PSP shows a type IV adsorption isotherm, suggesting the presence of both micro and mesoporosity.

The derived porosity parameters are compiled in Table 1. PSP shows higher values of apparent surfaces area (A_{BET}), micropore and mesopore volume than PSG. The NLDFT pore size distribution derived from the respective N_2 and CO_2 adsorption isotherms, Fig. 1B, confirms that the CO_2-activated carbon has developed a narrow microporosity, with >90% of the pore volume represented by pores of sizes below 1.2 nm and a maximum in the pore size distribution centered at 0.65 nm (see inset on Fig. 1B). However, the chemical activation of PS with H_3PO_4 has rendered a porous carbon (PSP) with a bimodal pore size distribution, also showing a sharp peak corresponding to micropores, with a maximum centered at 0.9 nm, and an asymmetric broadband showing a maximum for the pore size at 1.2 nm, a wide shoulder from 2 to 5 nm, which accounts for 24% of the distribution, followed by a long tail that covers 57% of the pore volume up to pore size of 20 nm. In addition, XRF and XPS analyses of the chemically activated carbon support clearly confirmed the presence of P surface species (0.8 and 1.4% wt., respectively). In sum, the disparity between the PSD of the two carbon supports and the presence of phosphorus in PSP are expected to have a strong impact on the dispersion and chemical state of the nickel in the final carbon-based catalytic systems.

Table 1 summarizes the most relevant parameters of the nickel catalysts supported on the chemically (PSP-Ni) and physically (PSG—Ni) activated carbons. After the impregnation with the metal phase, the porosity of the resulting catalysts was modified. In the case of PSG—Ni, the decrease in surface area, micropore, mesopore and total volume was ca. 10%, suggesting that nickel has been preferentially deposited on the external surface of the particles, without any significant filling of the micro- or mesoporosity. Differently, the comparison of the textural parameters of PSP support and PSP-Ni catalyst reveals a homogeneous reduction of the porosity parameters of ca. 30%. Most of the decrease on textural parameters can be associated to the porosity shrinkage caused by the thermal treatment at 700 °C, Fig. S2, although the possibility of a porosity blockage by nickel cannot be ruled out. Comparisons between the pore size distribution of PSP and PSP-Ni, Fig. 1B, confirm the shrinkage of porosity in the 1–15 nm range, with the largest decrease being found for pore widths of 2–5 nm. In addition, although both catalysts have similar Ni contents determined by XRF, the XPS nickel surface concentration is much lower in PSP-Ni than in PSG—Ni, Table 1, pointing out that a relevant fraction of the active phase has been loaded within the porosity of PSP-Ni.

Table 1
Characterization of catalysts.

	PSP	PSG	PSP-Ni	PSG-Ni
N_2 adsorption-desorption isotherm at −196 °C				
A_{BET} (m^2/g)	1400	965	975	895
Vs (cm^3/g)	0.44	0.36	0.29	0.34
V_{meso} (cm^3/g)	1.16	0.05	0.85	0.06
V_{tot} (cm^3/g)	1.60	0.41	1.31	0.41
XRF composition (wt%)				
P	0.9	0.0	1.5	0
Ni	0	0.0	13.4	10.7
XPS composition (wt%)				
C	90.9	91.4	93.0	78.8
O	7.7	8.6	4.4	10.8
P	1.4	0.0	0.8	0.0
Ni	0.0	0.0	1.9	10.4
Acidity (TPD-NH_3)				
NH_3 (mmol/g)	0.23	n.m.	0.07	n.m.

n.m.: not measured.

Compositional data analyses by XRF confirmed nickel loadings of around 11 and 13%wt. for PSG-Ni and PSP-Ni catalyst, respectively. The higher nickel concentration in PSP-Ni can be related to the preparation temperature of the support, 500 °C. Since the catalyst is annealed at 700 °C, additional weight loss from the support takes part between 500 and 700 °C due to the decomposition of surface oxygen groups such as anhydrides and phenols [30]. In addition, H_3PO_4 activated carbons are known to have phosphate and polyphosphate functional groups on their surface [31]. These phosphorus groups could be able to react with nickel, forming nickel phosphide species. The support would provide carbon atoms as reducing agent, releasing CO, and therefore bringing additional weight loss of the support, increasing the concentration of the inorganic fraction of the catalyst (i.e., Nickel). The formation of nickel phosphide seems to be confirmed by XPS analyses, Fig. 2. Detailed analysis of the P2p photoemission region (Fig. 2A) shows a wide band at 133.2 eV related to the presence of C-O-P bonds and a narrow band at 129.5 eV that has been ascribed to the formation of nickel phosphide ($P^{\delta-}$) [50]. The XPS core level spectrum of Ni2p is reported in Fig. 2B. The spectrum of PSG-Ni shows two clear bands centered at 852.5 and 856.0, indicative of metallic nickel (Ni) and oxidized species such as

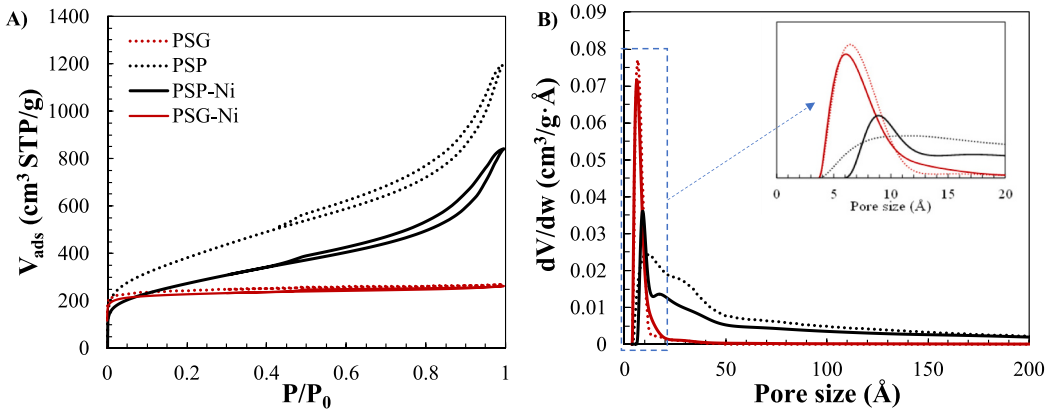

Fig. 1. A) N_2 adsorption-desorption isotherms at −196 °C of the PSG-Ni and PSP-Ni catalysts and the parent supports (PSG & PSP, respectively). B) NLDFT Pore size distribution derived from the N_2 and CO_2 adsorption isotherms at −196 °C.

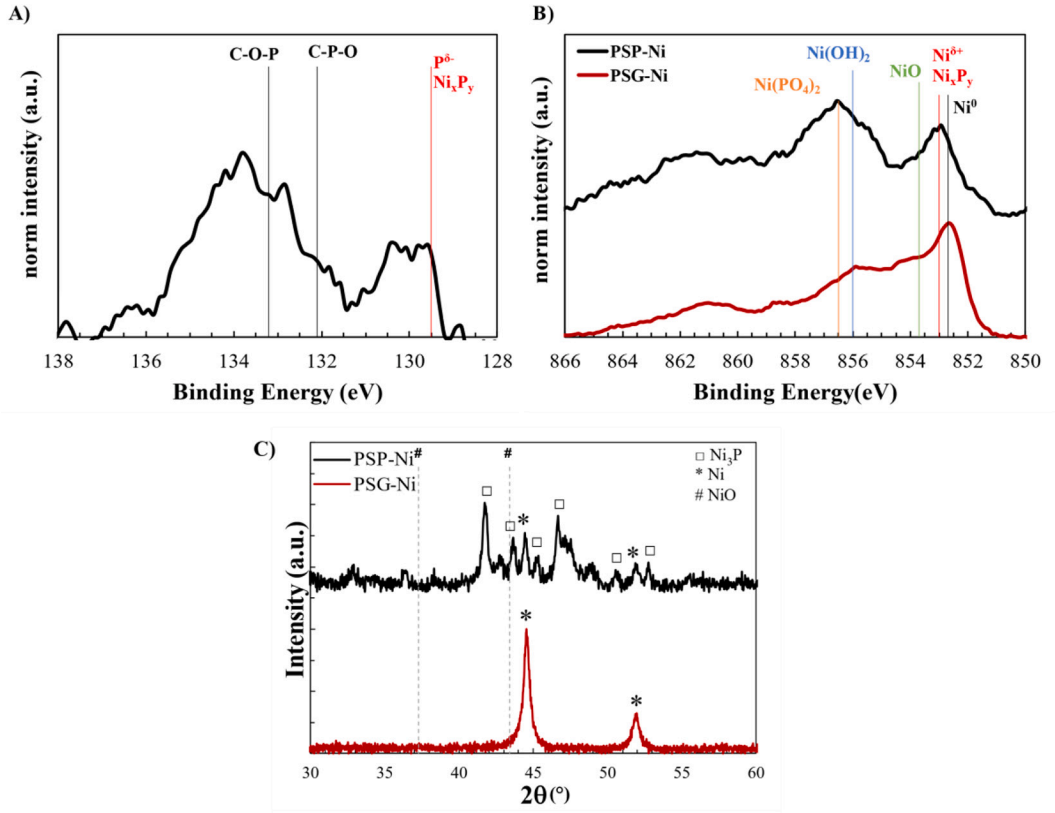

Fig. 2. A) P2p XPS region of PSP-Ni catalyst. B) Ni2p XPS photoemission region of PSP-Ni and PSG-Ni catalysts. C) XRD of PSG and PSP catalysts.

oxyhydroxides (NiO_x), respectively, and a shoulder at 853.7 eV related to the presence of NiO species [50–52]. PSP-Ni catalyst shows some change on these peaks. The first one is now found at 853.0 eV, suggesting the presence of Ni species with a small amount of positive charge ($Ni^{\delta+}$), while that related to NiO is no longer found, whereas the one ascribed to NiO_x species is increased and displays a positive shift to 856.5 eV, possibly related to the interaction with remaining phosphate ions and/or other surface oxygen groups [53], which are not found on the PSG support.

Deconvolution of Ni2p XPS region spectra, Fig. S3, allows to determine the presence of each nickel specie in the catalysts, whose relative areas are given in Table S1. According to these fits, about 35% of the nickel in PSG-Ni is Ni^0, the remainder being nickel oxides that can be reduced to metallic nickel. In PSP-Ni, P-related compounds represent approximately half of the nickel species.

The formation of nickel phosphide species in PSP-Ni has been also corroborated by XRD, Fig. 2C. The XRD pattern of the PSG-Ni catalysts shows diffraction peaks at 2θ values of 44.4 and 51.8, attributed to the presence of metallic nickel phase, confirming the formation of Ni^0 species observed on the catalyst surface by XPS. The PSP-Ni XRD pattern also shows the diffraction peaks corresponding to crystalline nickel, although they are less intense than those related to the presence of Ni_3P (see square dots in Fig. 2C). The preferential formation of Ni_3P over other phosphides with lower Ni/P ratio can be understood attending to the weight ratio of nickel and phosphorus that are put together during the preparation of the PSP-Ni catalyst. Ni_3P requires a value of 5.7 for Ni/P weight ratio, whereas the PSP + $Ni(NO_3)_2$ mixture used in the catalyst synthesis shows a value of 11.1 for Ni/P weight ratio, favoring the formation of Ni_3P over any other higher P-containing phosphide species. It should be noted that the synthesis of nickel phosphides usually requires the reaction of toxic gases as phosphines with metals, the reduction of metal phosphates by hydrogen, the use of plasma treatments or the thermal decomposition of precursors using long reaction times and high reaction temperatures (in the range of 1000 °C) [54]. To our knowledge, this is the first time that the production of nickel phosphides species through a straightforward thermal treatment procedure using as P-donating agent a H_3PO_4-activated biomass source is ever reported in the literature. The decrease on the acidity of the PSP-Ni catalyst, as denoted by the NH_3-TPR values for PSP-Ni and PSP samples in Table 1, also confirms the loss of surface C-O-P groups, which are responsible for the acidity of P-containing activated carbons [55].

H_2-TPR analyses of the catalysts are shown in Fig. S4A-B. PSP-Ni H_2 consumption profile consists of two peaks at 330 °C and 480 °C that may be related to the reduction of free NiO and NiO particles with strong interaction with the support (which made them less prone to be reduced), respectively [56]. The small evolution of CH_4 at 350 °C can be related to the reduction of amorphous polymeric carbon species on top of nickel species, a conventional feature of Ni catalysts that has been exposed to hydrocarbons under reductive atmosphere at high temperatures [57]. These amorphous carbon deposits can be formed during the annealing treatment of the catalyst at 700 °C. The evolution of H_2O (18 *m/z* line on Fig. S4A) from the reduction of nickel oxide is much higher. Given that mostly H_2O evolution was registered on that temperature range, the H_2 consumption registered for PSP-Ni mainly corresponds to reduction of nickel oxides particles. In the PSG-Ni catalyst, the higher and broader H_2 consumption profile might be interpreted as the reduction of nickel oxide starting at lower temperatures and proceeding over a wide range of temperature than for PSP-Ni, Fig. S4B. However, it is noteworthy the rise of the 15 m/z, related to methane evolution from the catalyst, at 250–350 °C, probably due to the reduction of amorphous carbon. Another large methane peak is registered at 530 °C, evidencing that a relevant fraction of hydrogen has been consumed by the methanation reaction of CO_2 evolving from the surface of the PSG-Ni support, which is catalyzed by nickel catalysts [56]. In addition, hydrogen can be consumed in the methane formation for the PSG-Ni catalyst, therefore the amount of reducible nickel has been estimated from the H_2O

evolution for both samples. The results show a hydrogen consumption of 0.68 mmol/g for PSP-Ni and 1.01 mmol/g for PSG—Ni, pointing out that PSG-Ni catalyst has a larger amount of nickel oxide species. In fact, considering that all phosphorus in PSP-Ni catalyst is forming Ni_3P, only 8.9% wt. of metallic nickel would be found in PSP-Ni, versus the 10.7% shown by PSG—Ni. In view of the H_2-TPR results, a hydrogen reduction treatment at 600 °C prior the steam reforming experiments with PSG-Ni has been established to achieve full reduction of the active phase.

TEM images from PSG-Ni and PSP-Ni catalysts are gathered in Fig. 3. The PSG-Ni images reveal a distribution of nickel particles with sizes ranging from 10 to 40 nm, Fig. 3A. Most of them seem to be placed on top of the carbon particles, suggesting that the average diameter of the Ni particle is larger than the mean pore size of PSG—Ni, Fig. 1B. PSP-Ni catalyst shows a less dense structure of the carbon support, along with the presence of metal nanoparticles with a broader size distribution, Fig. 3B. A detailed HR-TEM analysis of these nanoparticles on PSP-Ni shows a clear crystalline structure, Fig. 3C, in which the observed interplanar spacing (0.205 nm) corresponds to metallic nickel. In addition, EDX analysis of different metal nanoparticles reveals large domains containing nickel and phosphorus (Fig. 3D), confirming the presence of nickel phosphide, along with small nickel regions which are free of phosphorus (see white circles in Fig. 3E-F). These results suggest that nickel in PSP-Ni is distributed between Ni_3P and, in less extend, metallic nickel species.

3.2. Steam reforming of model bio-oil compounds

Bio-oil is a complex mixture of organic compounds and water. The composition and yields of the different fractions obtained from pyrolysis of pistachio shell have been recently reported [48,58]. Fig. 4A shows the composition of a bio-oil obtained from fast pyrolysis of pistachio shell at 500 °C. The aromatic fraction is regarded as an interesting value-added product; however, it needs to be upgraded through purification processes [59]. The aqueous fraction of biomass pyrolysis liquids has been envisaged as ideal source of hydrogen [60,61]. Ethanol extraction of bio-oil can be useful to obtain a raffinate concentrated in phenols and other oxygenated aromatics. The resulting ethanol extract is rich in acids, water, ketones/aldehydes and ethanol, Fig. 4B, having an adequate composition to produce hydrogen through steam reforming. Bearing this composition in mind, a mixture of ethanol, acetone, acetic acid in equimolar ratios has been prepared and used as model compounds for steam reforming using the PSP-Ni and PSG-Ni catalysts, adding water in a stoichiometric ratio.

Gasification of the support is one of the main drawbacks of using activated carbons as supports for the preparation of catalysts. In this sense, when only water was feed to the reactor inlet at 700 °C (at the same H_2O molar flow value later used in the steam reforming of model compounds), the catalysts provided a relevant weight loss that is related to the gasification of the carbon supports. After 20 h of TOS, burn-off values of 83.9 and 36.8% were obtained for PSG-Ni and PSP-Ni, respectively, suggesting that the activated carbon prepared by chemical activation with H_3PO_4 delivers a higher resistance to steam gasification. Indeed, phosphorus groups provide higher oxidation resistance due to the preferential formation of phosphate groups on carbon free sites and the high thermal stability of C-O-P bonds [44]. Moreover, the inhibition effect of phosphorus on the steam gasification of chars from lignocellulosic origin has been connected in the literature with the formation of phosphates, suppressing the catalytic activity towards gasification [62]. Both phenomena could explain the higher resistance towards gasification of PSP-Ni. In spite of the gasification of the carbon

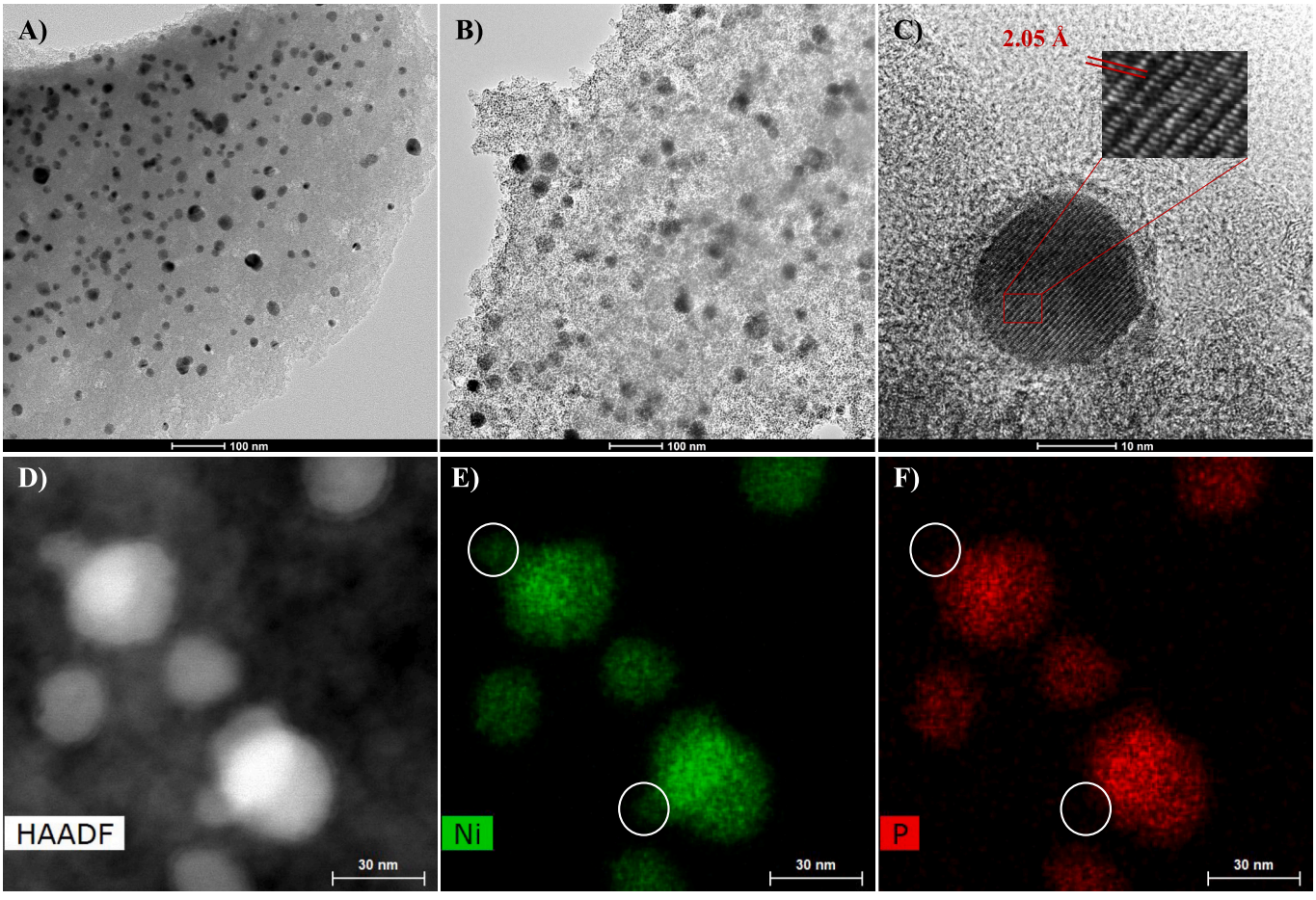

Fig. 3. TEM images of A) PSG-Ni and B) PSP-Ni catalysts. C) HR-TEM of PSP-Ni. D-F) HAADF & EDX Ni and P mapping image of metal nanoparticles from PSP-Ni.

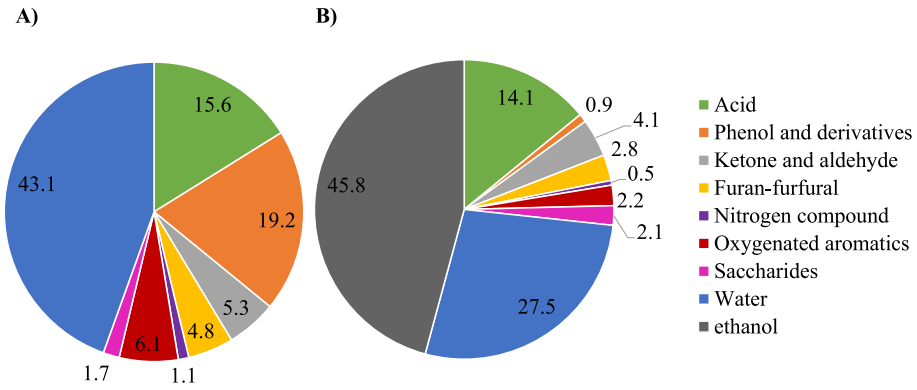

Fig. 4. A) Composition of the bio-oil fraction. Adapted from [45]. B) Composition of ethanol extract obtained with 1:1 *v*/v ethanol/bio-oil.

supports, the evolution rate of H_2, CO and CO_2 are at least two orders of magnitude lower than the one measured during steam reforming experiments (see PSG-Ni-H_2O and PSP-Ni-H_2O columns in Table 2), allowing to discard the potential contribution of gasification to the gas evolution during the reaction.

The steam reforming of the model compounds has been carried out at 600 and 700 °C for both PSG-Ni and PSP-Ni catalysts under the same inlet concentration (0.75% v/v for the model compounds and 7.5% v/v water) and space time conditions (50 g_{cat}·s/mmol). Fig. 5 shows the corresponding conversion and gas product distribution at the reactor outlet. Conversions only reached values of 7–8% for acetic acid and acetone, and slightly over 25% for ethanol at 700 °C, being almost negligible at 600 °C in the absence of catalyst. Much higher conversions of all the model compounds are achieved in the presence of Ni catalysts, confirming the high steam reforming activity of both catalysts. The main gaseous reaction products are hydrogen and carbon monoxide. The formation of ethylene in small amounts can be associated to the dehydration reactions of ethanol, while CO_2 production is related to the water gas shift (WGS) reaction between carbon monoxide and steam. H_2, CO and CO_2 concentrations limits at 600 °C according to thermodynamic equilibrium are 9.3, and 2.6 and 2.1%, respectively. It is observed that ethanol and acetone conversion are slightly higher for PSG-Ni catalyst at 600 °C, along with hydrogen and carbon dioxide concentrations. PSP-Ni catalyst seems to favor methane formation at the cost of small decrease on hydrogen production.

At 700 °C, the conversion values are around 90% for all the model compounds in the case of PSG-Ni and close to total conversion for PSP-Ni catalyst. At this temperature, the product distribution is notoriously affected by the catalyst. The obtained H_2, CO and CO_2 concentrations are within the thermodynamic equilibrium limits at 700 °C (9.4, 2.9 and 1.9%, respectively) for the set of reactions depicted in Eqs. (1)–(3). H_2 production is maximized for PSG—Ni, while the formation of methane seems to be minimized. Differently, PSP-Ni shows a lower hydrogen concentration, a higher H_2/CO ratio, but also a notable formation of methane. The steam reforming of ethanol, acetone and similar bio-oil derived oxygenate compounds proceeds through a series of competing reaction pathways, namely i) dehydrogenation of the compound followed by steam reforming of the resulting oxygenated intermediates, producing hydrogen and carbon monoxide, with water gas shift delivering the formation of CO_2; ii) the side dehydration and decomposition reactions, which produces undesired ethylene, methane and coke deposits. In this side pathway, methane can be reformed with steam by nickel catalysts when reaction temperature is high enough; iii) hydrogenation of CO and CO_2, generating additional CH_4 [63–65]. In this sense, nickel phosphide is regarded as an active hydrotreatment catalyst [66], and has been tested as hydrodeoxygenation catalyst for bio-oil upgrading [67]. Therefore, it could enhance the methanation rate of PSP-Ni with respect to that of PSG—Ni. The carbon mass balance reveals that, of the carbon consumption in PSP-Ni, 32% can be attributed to CH_4 production, while 66% is associated with the steam reforming/inverse WGS reaction pathway (estimated from the generated amount of CO and CO_2). These percentages align reasonably well with the presence of 53% nickel phosphides and 47% metallic nickel as calculated from XPS data, pointing out a likely relationship between the presence of nickel phosphide and the methanation reaction. The differences in the extent of each reaction and the concentration of active phases could be related to the weaker catalytic activity of the nickel phosphides. Ni_2P is also reported to have a relevant activity for the dry reforming of methane with CO_2, although this reaction proceeds at higher temperatures (800 °C) [8], so probably it is not modifying the product distribution of PSP-Ni.

The catalytic performance at long time on streams (TOS) is the main concern when using carbon-based supports in this reaction. To obtain a better understanding of the enduring stability of the catalysts developed in this study, PSG-Ni and PSP-Ni were submitted to harsh reaction conditions (700 °C, S/C stoichiometric ratio in the gas inlet that favors coke deposition) for 50 h. Fig. 6 reports the evolution of conversion and gas outlet composition with TOS for steam reforming of the bio-oil model compounds at 700 °C using PSP-Ni and PSG-Ni catalysts, respectively. The conversion and composition of the gas outlet at TOS of 5 and 50 h has been also gathered in Table 2. It can be seen that the activity of the catalysts is affected by TOS. Initially, acetone, ethanol and acetic acid conversions are close to 100% for both catalysts. PSP-Ni showed significant stability under the studied reaction conditions, keeping high conversion values throughout all the reaction time. Initially, PSG-Ni also showed high activity with near total conversion of the oxygenates, but conversion decreased from almost 100% to 40–50% in 15 h. From this TOS value, no signs of further deactivation were appreciated. The differences found in the catalytic performance for PSP-Ni and PSG-Ni during long time operation experiments were ascribed to the nature of the Ni active phases present on the surface of the carbon catalysts. PSP-Ni, contained nickel phosphide species on the its surface,

Table 2
Conversion (%) and outlet gas composition (% *v*/v) for the gasification & steam reforming experiments at 700 °C.

	PSG-Ni-H_2O[a]	PSP-Ni-H_2O[a]	PSG-Ni		PSP-Ni	
TOS[b]:	5 h	5 h	5 h	50 h	5 h	50 h
$X_{Acetone}$	n.a.	n.a.	80.4	45.7	94.8	77.4
$X_{Ethanol}$	n.a.	n.a.	85.2	48.9	87.8	79.8
$X_{AceticAcid}$	n.a.	n.a.	84.7	44.6	93.5	94.4
H_2 ($\%_v$)	0.004	0.029	3.864	2.385	3.579	3.271
CH_4 ($\%_v$)	0.009	0.010	0.106	0.134	1.102	1.094
CO ($\%_v$)	0.005	0.027	1.148	0.633	0.916	2.014
CO_2 ($\%_v$)	0.017	0.018	1.078	0.669	0.518	0.634
$C_2^=$ ($\%_v$)	0.000	0.002	0.020	0.050	0.009	0.092

n.a.: not applicable.
[a] only steam is feed on the gas inlet. C_{H2O} = 7.5% v/v.
[b] Time on stream.

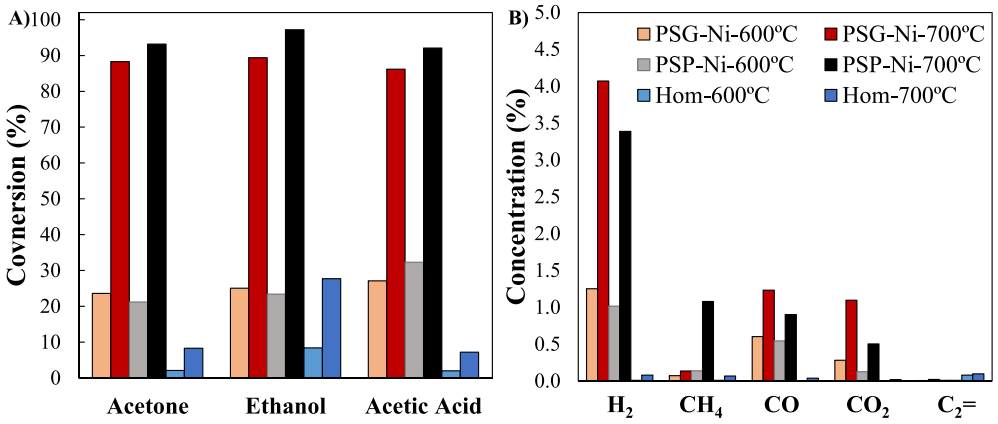

Fig. 5. A) Conversion and B) gas product distribution during steam reforming of model compounds at 600 °C and 700 °C using PSP-Ni and PSG-Ni catalysts. Time on stream: 1 h. Legend appearing in B) is shared for both panels.

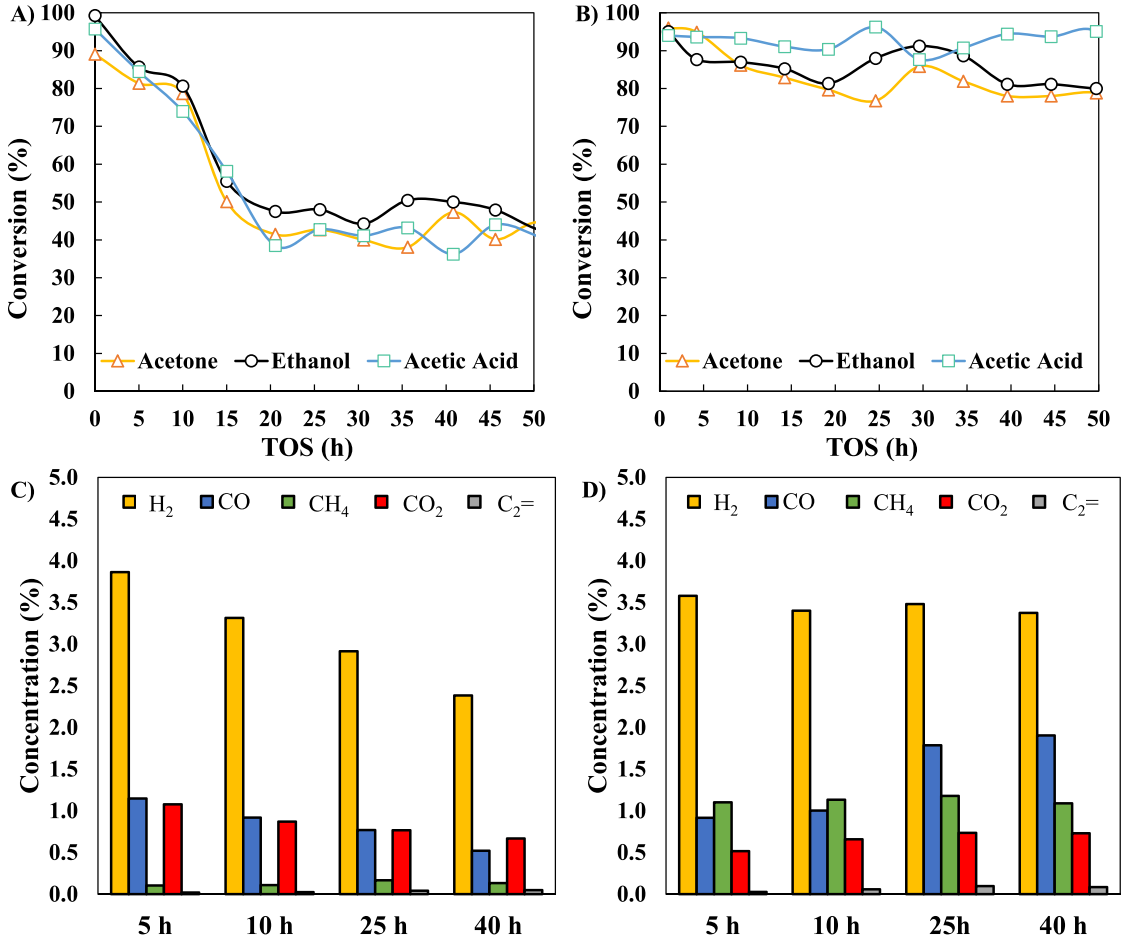

Fig. 6. Time on stream results during steam reforming at 700 °C. Conversion of acetone, ethanol and acetic acid using A) PSG-Ni and B) PSP-Ni catalysts. Gas outlet composition using C) PSG-Ni and D) PSP-Ni catalysts.

which hindered the formation of CNTs and, thus, the deactivation due to coke deposition. Conversely, the P-free catalyst, PSG-Ni presented NiO species on the catalyst surface, which promote CNTs formation under reaction conditions. This CNTs growth results in the partial deactivation of the catalyst. After 20 h on stream though, the catalyst showed a steady-state operation regime, in which highly active catalyst particles yielding CNTs were deactivated. These carbon nanotubes act as a new support for the Ni particles, allowing the reaction to take place for a long period of time, making operation stable. In the light of these results, it can be foreseen that both catalysts could perform stable for longer times on stream.

Accordingly, hydrogen, CO and CO_2 concentration decreases with TOS for PSG—Ni, Fig. 6C, whereas methane and ethylene increases, probably due to the lower activity of the catalyst for the steam reforming of methane. Interestingly, the CO/CO_2 ratio decreases from 1.1 to 0.9, indicating a lower contribution of the inverse WGS reaction, and consequently, the H_2/CO ratio improves from 3.37 to 3.80 at the end of the catalytic experiment. In PSP-Ni, the hydrogen production remains

remarkably stable, as in the case of methane. However, the product distribution is shifted towards higher formation of carbon monoxide, Fig. 6D, decreasing the H_2/CO ratio as well as the CH_4/CO one at the gas outlet, going from 3.91 down to 1.62 and from 1.20 to 0.54 at the end of the experimental run, Table 2. The low H_2/CO ratios and the presence of methane in the reactor outlet are clearly consequence of the low S/C value in the feed, which favors the inverse WGS reaction and hinders the rate of the steam reforming of methane. Inorganic catalysts with higher steam concentration in the gas inlet minimizes the methane formation and greatly enhances CO_2 formation. However, even when working at high S/C ratios, inorganic catalysts such as Ni/α-Al_2O_3 modified with La_2O_3 faces stronger deactivation than that found for PSP-Ni and even PSG-Ni catalysts under similar temperature and space time operation conditions [68].

Due to the lack of details provided by studies about the steam reforming of pyrolysis liquids and the wide variety of operating conditions, it is difficult to stablish straightforward comparisons of the conversion, selectivity and yields results obtained in this work. Therefore, the effectiveness of the catalysts has been evaluated by calculating their activity as consumed moles of reactant per hour and per mass of nickel at TOS of 5 h. Chen et al. and Di Stasi et al. analyzed the activity of 10% nickel-loaded catalysts supported by activated carbons in steam reforming of acetic acid at 700 °C using an S/C of 2.5 and 4, respectively [35,69], achieving activities of 1.29 and 1.42 $mol_{oxygenated}\cdot h^{-1}\cdot g_{Ni}^{-1}$, respectively, which were slightly lower than the value reached by the P-containing catalyst prepared in the present work, of 1.92 $mol_{oxygenated}\cdot h^{-1}\cdot g_{Ni}^{-1}$. Nevertheless, considering that only 47% of the total metal, according to deconvolution of the XPS data, after reducing is metallic nickel, PSP-Ni performed an activity referred to Ni^0 of 4.076 $mol_{oxygenated}\cdot h^{-1}\cdot g_{Ni0}^{-1}$. On the other hand, the 15%-nickel-loaded catalyst supported on a coal ash reported by Wang et al. was tested at S/C = 1 and 700 °C and showed an activity lower than 1 $mol_{oxygenated}\cdot h^{-1}\cdot g_{Ni}^{-1}$ [70]. It must be highlighted that the nature of the bio-oil can influence the catalytic activity, and the presence of additional compounds in the feed certainly has influence in the SR catalytic activity of PSP-Ni and PSG—Ni. These comparisons allow to stablish that these catalysts have SR activity in line to those found in the literature.

Regarding inorganic supports, Bimbela et al. tested nickel over Al_2O_3 catalysts in a wide range of conditions, such as reduction time, nickel loading and reaction temperature [71]. When using an S/C ratio of 5.58 and acetic acid as reactant, they reported an activity of 2.15 $mol_{oxygenated}\cdot h^{-1}\cdot g_{Ni}^{-1}$ by testing a 23%-Ni-loaded catalyst at 650 °C, whereas the 33%-Ni-loaded catalyst tested at 750 °C reached a value of 2.06. In addition, Basagiannis et al. reported an activity of 1.36 $mol_{oxygenated}\cdot h^{-1}\cdot g_{Ni}^{-1}$ when analyzing a 17%-Ni-loaded catalyst over Al_2O_3 and La_2O_3 at S/C = 3 and 700 °C [72]. Note that the advantage of inorganic supports is that they allow the use of higher S/C molar ratios, which improves the catalytic activity [68], while carbon supports would suffer from gasification when exposed to those S/C values due to the presence of excess of H_2O. Nevertheless, these catalysts are usually prepared with higher nickel loadings, which can lead to worse dispersion of the active phase and sintering of the nickel particles, and therefore their performance is only slightly better than the one achieved in this work using carbon supported catalysts.

It is important to point out that the evolution of the conversion and product distribution in the steam reforming of oxygenates is not usually studied for >2 h, due to strong catalyst deactivation. For instance, Zhang et al. analyzed the activity of Ni catalysts at 600 °C and S/C of 5, at different nickel loadings, reporting clear signs of deactivation from the first hour of reaction, for a 10% wt Ni/γ-Al_2O_3 catalyst [73]. Some of the above-mentioned works have performed a stability test of the catalysts for TOS of 10–12 h, showing similar deactivation to that found for PSG-Ni [17,35,70]. The use of stability promoters as lanthanum or yttrium are needed to achieve stable catalytic performances for time on streams comparable to those herein explored [39]. For example, Fatsikostas et al., proposed the use of La_2O_3 as support to achieve a stable catalytic performance for a TOS of 90 h in the steam reforming of ethanol, at 750 °C and S/C of 1.5 [74], therefore, the outstanding stability shown by the PSP-Ni catalyst without the addition of unconventional promoters must be highlighted.

The yields towards the different products obtained by steam reforming using PSG-Ni and PSP-Ni catalysts are reported in Fig. 7. Again, the high stability on hydrogen yield of PSP-Ni is remarkable, whereas clear signs of deactivation can be appreciated on the hydrogen yield of PSG—Ni. Similar deactivation trends are observed for CO and CO_2 on the latter catalyst, while methane and ethylene yields increase with TOS. Differently, PSP-Ni develops higher CO and CO_2 yields with TOS. Besides the evolution of gases, the negative carbon balance reveals that coke is deposited in both catalysts, especially at short TOS values, where estimated coke selectivity up to 38 and 34 wt% for PSG-Ni and PSP-Ni at TOS of 5 h were observed, respectively. The favorable adsorption, solubility, and diffusion of carbon on nickel during reforming reactions of both light hydrocarbons and oxygenates explain the fast coke formation on these catalysts [57]. Coke selectivity estimated from carbon balance diminishes with TOS for both catalysts. This decrease is more pronounced for PSP-Ni, which shows negligible coke selectivity from the carbon balance closure after 40 h. The used catalysts were recovered and weighted after TOS of 50 h to check the amount of coke formed. When referred to the inorganic matter present in the catalyst, a 272% weight increase for PSG-Ni was obtained, while PSP-Ni showed a lower weight increase (92%). This difference could be connected to the higher methane and carbon monoxide rate formation of latter catalysts.

The mechanism of coke generation involves the dissociative adsorption of light hydrocarbons on nickel, with highly active monoatomic carbon being gasified by steam to form CO and H_2. Given that a low S/C ratio has been used in this work to avoid the gasification of the catalytic support, the gasification rate of the deposited monoatomic carbon is low, favoring polymerization reactions that give rise to coke accumulation [75]. However, the coke formation can be inhibited by controlling the active sites available for the polymerization of monoatomic carbons. For instance, Alstrup and Andersen modified Ni catalyst with nickel sulfide, achieving NiS surfaces containing small regions of free nickel sites [76]. The presence of NiS delimited the Ni sites available for polymerization of monoatomic carbon. Consequently, coke formation notoriously declined, due to a lower steam reforming reaction rate. Thus, it is expected that Ni_xP can also inhibit coke formation through a similar mechanism. Moreover, given that nickel phosphides are highly active hydrogenation catalysts, their presence could also remove monoatomic carbon species through hydrogenation, decreasing the coke formation or at least shifting the formation of aromatic coke to aliphatic one, following an analogous process to that reported for La-modified Ni catalysts [39,74]. Indeed, a much higher methane formation is observed for PSP-Ni catalyst at all TOS, Fig. 6. This hypothesis is supported by Wang et al., which reported a strong decrease of coke formation for Ni:P ratios of 2–4 for alumina-supported nickel as dry reforming catalyst [41].

In order to corroborate the lower formation of coke due to the presence of Ni_xP species, the PSP-Ni catalyst was submitted to a hydrogen treatment at 600 °C for 2 h prior to the catalytic test. According to the literature, hydrogen treatment of mixtures of nickel and phosphorus precursors at temperatures over 600 °C has been used for the production of nickel phosphides [77]. When the hydrogen-treated PSP-Ni catalyst is submitted to the steam reforming of the model compounds at 700 °C under the same space time as those for PSP-Ni and PSG—Ni, the conversions of acetone, ethanol and acetic acid were 9.3, 53.9 and 58% at TOS of 5 h, which was remarkably lower. Interestingly, the conversion values at TOS of 40 h are 20.9, 48.1 and 39.0% for acetone, ethanol, and acetic acid, pointing out the high stability of this catalyst. As expected from the lower activity, the hydrogen production is lower, reaching gas concentration values of around 1.5%, with carbon monoxide as the other main product, Fig. 8A. The stability of the gas

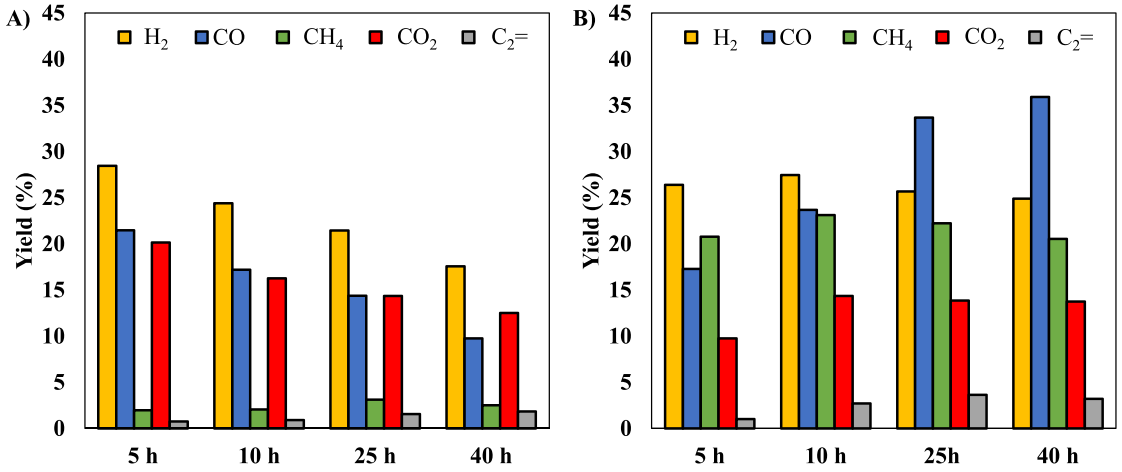

Fig. 7. Evolution of the yields to the main products at different TOS in the steam reforming experiments at 700 °C for A) PSG-Ni and B) PSP-Ni.

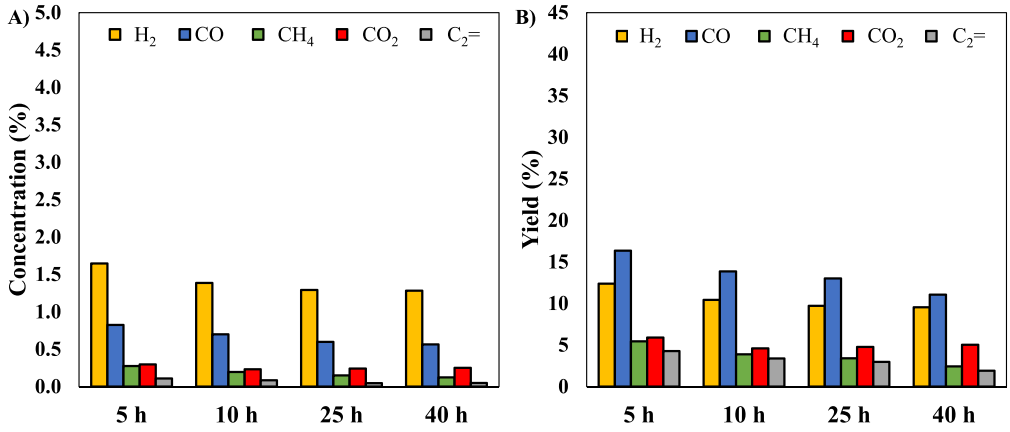

Fig. 8. A) gas concentration and B) yield evolution with TOS during steam reforming at 700 °C using PSP-Ni reduced in hydrogen for 2 h as catalyst.

outlet composition, however, is significantly greater than that exhibited by PSG—Ni. Similar performance in terms of stability is observed from the evolution of product yields with TOS, Fig. 8B. The outstanding stability of this catalyst is probably related to the low coke formation, as pointed out by estimated coke selectivity lower than 5%, being two-three times lesser than those registered by PSP-Ni and PSG—Ni.

3.3. Characterization of used catalysts

The used catalysts were recovered and submitted to characterization in order to identify the most likely origins of their different deactivation rates. Fig. 9 shows the TEM images of the used PSG-Ni and PSP-Ni catalysts at TOS value of 50 h. Clear evidence of metal sintering can be identified from the images of PSP-Ni, Fig. 9A, resulting in the most frequent average particle size increasing from 23 to 35 nm in relation to the fresh catalyst, Fig. S5, along with the formation of multi-walled-carbon nanotubes (CNTs) and some pyrolytic deposits on top of the catalyst. Even so, it should be noted that nickel continues to show high dispersion on the used catalyst. The size of the pyrolytic deposits in the form of large, bulky filaments and the amount of CNTs is drastically intensified in the case of PSG-Ni catalyst, Fig. 9B. The formation of coke deposits and carbon nanotubes in the presence of hydrocarbons at 700 °C is a well-known feature of nickel catalysts [78,79]. The formation of CNTs during steam-methane reforming at 500–600 °C is a well-known process, where the interaction between Ni^{2+} species, alkali promoters and support, as well as the size of the nickel nanoparticles are reported to play a major role; in fact, the use of impregnation methods to load the metallic phase delivers a promoted formation of CNTs [80]. Recently, Kontchouo et al. studied the formation of coke and carbon nanotubes in the steam reforming of several oxygenates, reporting that ethanol and acetone as feedstocks render the formation of thick wall, rough surface & tip-open CNTs, while long waist CNTs with smooth surfaces and active nickel-on-tip particles are achieved via acetic acid steam reforming [81]. In this sense, higher magnification TEM images of used PSG-Ni reveal that pyrolytic deposits are formed on the surface of carbon nanotubes, Fig. 9C, whereas the carbon support seems to have disappeared. EDX analyses confirms that the denser, bulky microfilaments observed in PSG-Ni images are indeed coke (carbon deposits), with some nickel nanoparticles being loosely dispersed on them, Fig. 9D-F. These analyses also reveal severe sintering of Ni particles, Fig. 9F. The different evolution of the catalysts structure between used PSG-Ni and PSP-Ni is also manifested by nickel particle size distributions at different TOS, Fig. S5. As previously mentioned, the nickel particles in PSP-Ni increase their most frequent sized to 35 nm after 50 h, while the distribution curve preserves the initial width, although it is fully shifted to higher nanoparticles sizes. In contrast, two different nickel particle size ranges can be appreciated for used PSG-Ni at TOS of 50 h. This first one, centered around 17 nm, is related to particles responsible for CNTs growth, which somehow managed to keep the initial particle size distribution of the fresh PSG catalyst. On the other hand, 24% of the size distribution corresponds to the sintered nickel particles inside the massive pyrolytic carbon structures (as those observed in Fig. 9), showing sizes from 40 to 100 nm. A 9% of the total measured Ni nanoparticles showed sizes even larger than 100 nm and have been excluded of Fig. S5 for clearness. This

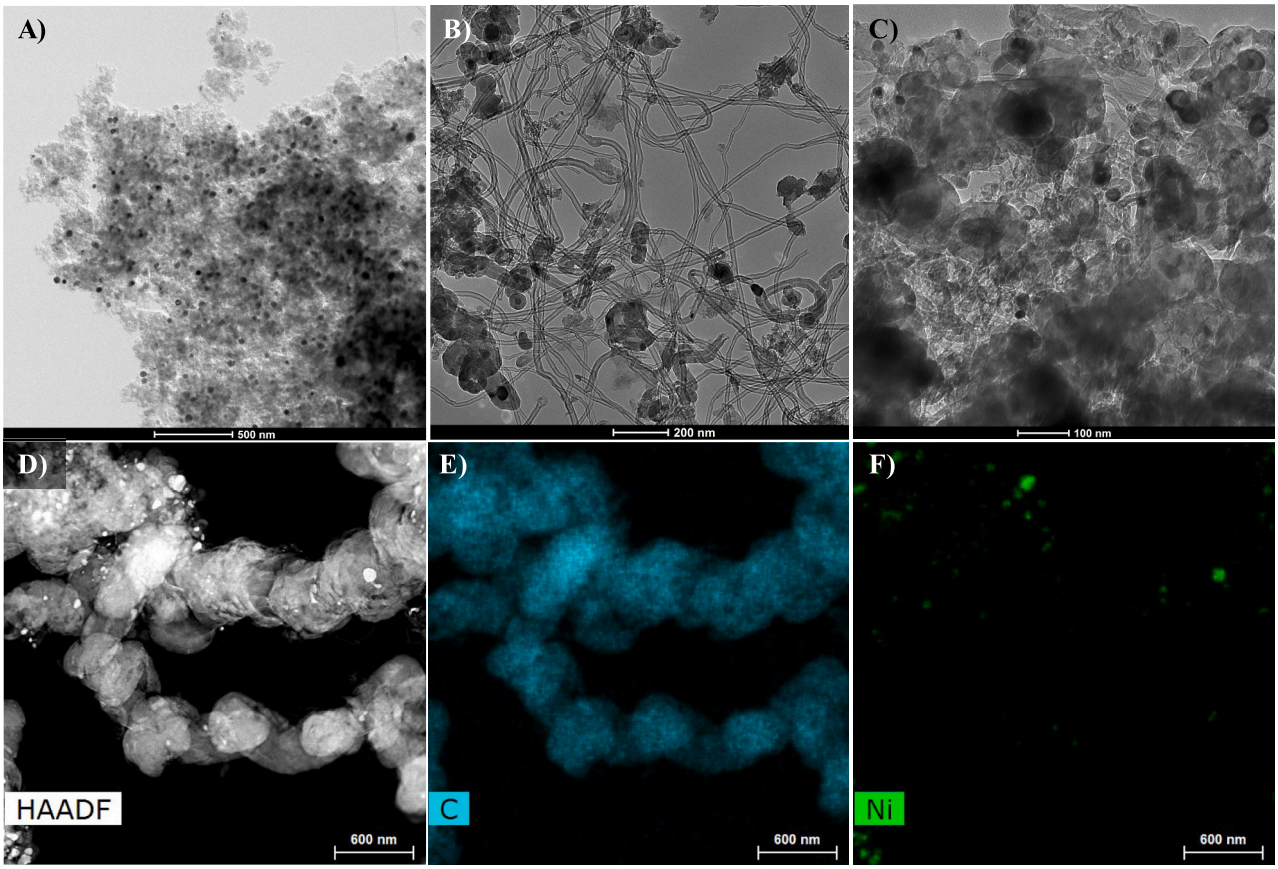

Fig. 9. TEM images of A) used PSP-Ni at TOS: 50 h and used PSG-Ni catalysts at B) TOS: 20 h and C) TOS: 50 h. D-F) HAADF & EDX C and Ni mapping image of used PSG-Ni catalyst.

result seems to point out that the smaller Ni nanoparticles preserve their average size, and probably their activity, due to the stabilizing effect of the formation of carbon nanotubes.

The formation of pyrolytic carbon and CNTs has also been checked by Raman spectroscopy, Fig. S6. Both PSG-Ni and PSP-Ni fresh catalysts show two intense peaks corresponding to the D and G bands at ca. 1320 and 1590 cm^{-1}, related to the presence of disordered carbon and graphite like structure, respectively, in the carbon supports. It is also possible to detect in the overtone region the 2D band at 2700 cm^{-1} and the D + G band at 2940 cm^{-1}, showing slightly narrower and more intense bands for PSG-Ni catalyst due to the higher preparation temperature of the activated carbon support (800 °C for PSG vs 500 °C for PSP, see experimental section), which favors the advance of structural order [82]. In the case of the used PSP-Ni catalyst (TOS of 50 h), the D band intensifies and gets narrower, suggesting the formation of amorphous coke [83], while the peaks on the Raman overtone region gets a better definition, yet with only a small increment on their intensity, Fig. S6A.

Differently, used PSG-Ni catalyst shows the opposite behavior, Fig. S6B, namely i) narrowing and shifting of the G band towards that of the 1584 cm^{-1} (see the detailed first tone Raman region on Fig. S6C), a position characteristic of graphene-like materials; ii) strong development of 2D band that achieves an intensity comparable to those of the D and G band. All these phenomena are proving the formation of an ordered carbon structure on the used PSG-Ni catalyst. In fact, the development of the 2D band is one of the features used for tracking the purity of multiwalled-carbon nanotubes [84]. Thus, Raman spectra confirms the preferential formation of carbon nanostructures on PSG—Ni, whereas the loss of disordered-related bands could be also interpreted as a proof of the gasification of the low-ordered PSG carbon support. The formation of CNT is probably inhibited in PSP-Ni due to the hydrogenation activity of nickel phosphide, favoring the formation of aliphatic coke over aromatic one. In addition, a detailed study about the catalytic growth of CNT using nickel nanoparticles supported in silica shown the formation rate is much lower when CH_4 is used as carbon source instead of CO [85], so the preferential formation of methane over CO in PSP-Ni catalyst is another factor contributing to attain lower carbon nanotube formation, avoiding catalyst deactivation. Ideally, the formation of CNT does not deactivate the catalyst since the nickel surface can keep adsorbing and diffusing carbon atoms for a long period of time, explaining the long-term activity of PSG—Ni, Fig. 6.

The nature of the coke recovered from the used catalysts after TOS of 20 h was analyzed by temperature programmed oxidation, Fig. 10. It can be observed that the reaction profile of the used PSP-Ni has been slightly shifted to a higher onset temperature in relation to the fresh catalyst. This change is much more pronounced in the case of PSG—Ni, where the starting of weight loss, attributed to the combustion of carbon, is delayed from 350 to 600 °C. The drastic differences between the TGA profiles of fresh and used PSG-Ni along with the loss of the support, pointed out by TEM images, suggest that a total gasification of the carbon support is attained after TOS of 20 h, evidencing the transformation of PSG-Ni into a new carbon nanotubes-based catalyst with a higher resistance to gasification. This structural modification is undoubtedly connected to the previously mentioned change in the conversion behavior at TOS of 15-20 h, Fig. S6, revealing that carbon nanotubes also provide a high and stable catalytic activity. In fact, Ni supported on carbon nanotubes have been successfully used as catalysts for the steam reforming of glycerol, although they operated at much lower temperatures [86].

XPS were recorded for the used catalysts at TOS values of 12 and 50 h, Fig. 11. The detailed analyses of the Ni2p region show that nickel surface amount is gradually decreasing with TOS for the PSP-Ni catalyst

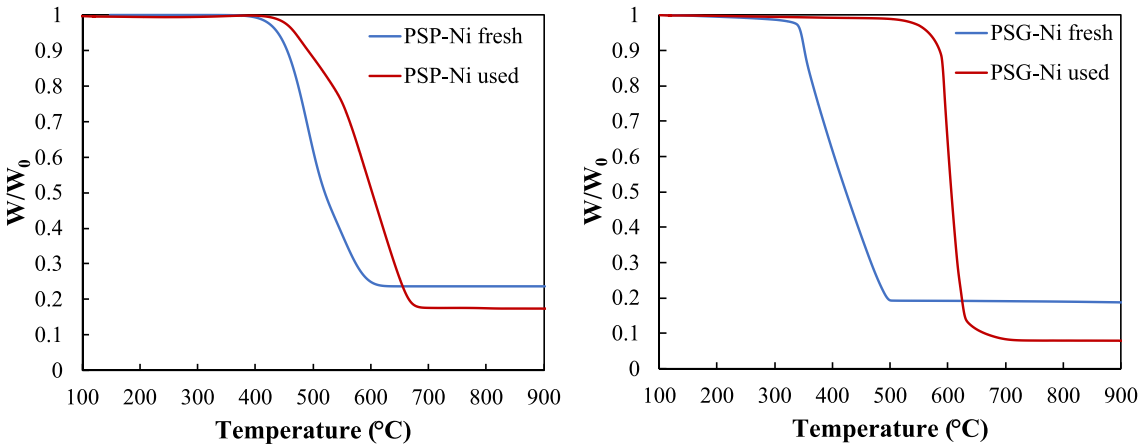

Fig. 10. Temperature programmed oxidation of fresh and used A) PSP-Ni and B) PSG-Ni catalysts. Heating rate: 10 °C/min.

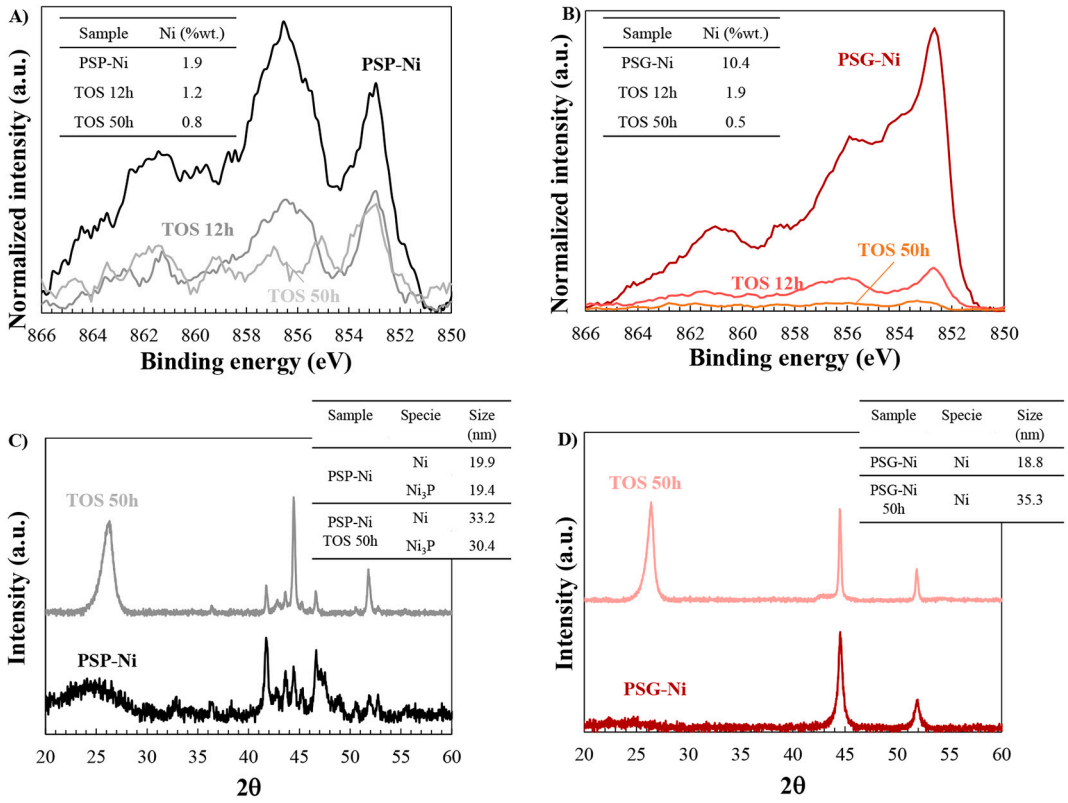

Fig. 11. XPS Ni 2p photoemission region of A) PSP-Ni and B) PSG-Ni fresh & used catalysts. XRD of C) PSP-Ni and D) PSG-Ni fresh & used catalysts.

(see inset with surface nickel content on weight basis on Fig. 1A). In addition, the peak at 856.5 eV progressively decreases, indicating that nickel oxides and phosphates could be gradually reduced. According to the XPS Ni2p spectrum of fresh and used PSG—Ni, this catalyst shows a strong decrease on surface nickel content after 12 h (~ 80%), achieving a lower value than that of PSP-Ni at TOS of 50 h (0.5% vs 0.8% for PSG-Ni and PSP-Ni catalysts, respectively), in agreement with the formation of large amounts of pyrolytic deposits and carbon nanotubes revealed by TEM images.

XRD patterns of the used catalysts at TOS 50 h are depicted in Fig. 11C-D. The used catalysts show a strong peak at 25.6°, which is attributed to the reflection of the (002) graphite crystal plane. An interplanar distance of 0.35 nm is derived from this reflection, pointing out a dense packing of graphene layers, quite close to the interlayer spacing of graphite (0.334 nm). This peak is especially narrow and intense for the used PSG-Ni catalyst at TOS of 50 h, confirming the formation of highly ordered carbon structures. In the case of PSP-Ni, apart from the reflections related to the presence of Ni_3P, the appearance of two narrow peaks can be observed at 2θ of 45° and 52° corresponding to crystalline Ni^0. The emergence of these peak reflections indicates that nickel species have been either reduced to Ni^0 or sintered during the reaction, confirming the findings of the TEM and XPS measurements. In fact, a significant sintering of the nickel species is observed for both catalysts, as revealed from the average crystal sizes determined from the Scherrer equation (see insets in Fig. 11C & D).

The porosity of the support is another factor that has influence on the deactivation of Ni catalysts. The formation of coke can usually produce the catalyst failure by plugging of the porosity of the support and the catalytic bed [87]. The presence of mesopores with large volumes in PSP-Ni may allow to allocate higher amounts of coke before full

blockage of porosity, increasing the lifetime of the catalyst. In this sense, Buentello-Montoya et al. studied the effect of the porosity on the performance of a biochar as support for the steam reforming of tar [88]. The authors concluded that the coke deposited in the porosity of mesoporous chars can be easily gasified by steam, while microporous supports showed initial higher activity, but faced a faster deactivation rate. The nitrogen adsorption-desorption isotherms of both used PSP-Ni and PSG-Ni show a clear decrease on the nitrogen uptake at low and medium pressures, evidencing the porosity blockage generated by the deposition of coke and the possible gasification of the carbon support, Fig. 12A-B. The used PSP-Ni catalyst still retains superior textural properties due to the presence of a large mesoporosity system on the fresh catalyst. However, the used PSG-Ni catalyst develops a new hysteresis loop on the N_2 adsorption-desorption isotherm at relative pressures over 0.8, Fig. 12B. The NLDFT pore size distribution of this sample shows the formation of mesopores, with size distributions centered at approximately 10 and 33 nm, Fig. S7B, which are hardly observed in the PSD of the PSP-Ni used catalyst obtained at a similar TOS, Fig. S7A. These mesopore sizes are in good agreement with the average inner diameter of the CNT observed in TEM images and the confined pores formed in the aggregated structure of CNT bundles [89], corroborating the preferential formation of carbon nanotubes on PSG-Ni catalyst.

In sum, catalyst deactivation seems to proceed through nickel sintering and carbon deposition. PSG-Ni catalyst seems to face both deactivation mechanisms, and also suffers from the gasification of the catalyst support, which probably enhances nickel sintering. However, the presence of mesopores and Ni_xP species on PSP-Ni partially inhibits the latter deactivation mechanism, explaining the superior stability of PSP-Ni at long time on streams.

4. Conclusions

Nickel catalysts have been prepared using activated carbons (ACs) obtained by CO_2 and H_3PO_4-activation of pistachio shells. The characterization shows that catalysts with large specific surface area (close to 1000 $m^2 \cdot g^{-1}$) well developed micro- and mesoporosity and homogenously dispersed nickel nanoparticles have been obtained. Nickel nanoparticles seem to be as metallic nickel, nickel (I) and (II) oxides in the CO_2-activated carbon. XPS, XRD and TEM-EDAX suggest that the presence of surface phosphorus on the H_3PO_4-activated carbon leads to the additional formation of nickel phosphide species on the P-containing catalyst. Both catalysts have demonstrated remarkable activity for the production of hydrogen through steam reforming (SR) of acetone, ethanol and acetic acid (model compounds of the aqueous bio-oil fraction of pyrolysis of pistachio shells) using low steam to carbon ratios, achieving near 100% conversion at 700 °C. Time on stream analyses on SR at 700 °C up to 50 h revealed that the Ni catalyst prepared from the P-containing AC support shows a stable catalytic activity after 50 h, producing a gas mixture mainly composed by H_2, CH_4, CO and CO_2. Differently, a lower CH_4 formation, as well as a decline in SR activity during the first 20 h on stream is observed when the CO_2-activated support is used. From that point, the catalyst shows a steady catalytic performance, preserving the activity and a superior H_2/CO ratio up to 50 h. The higher stability of the P-containing catalyst seems to be connected to the promotion of methanation reactions by the presence of nickel phosphides, which suppresses coke formation.

The characterization of the catalysts after TOS of 20-50 h reveals that deactivation of the CO_2-activated catalyst is related to the support gasification, leading to the partial sintering of the active phase, and massive coke deposition, while the remaining activity seems to be related to the formation of carbon nanotubes, that stabilizes nickel nanoparticles, obtaining a stable and highly selective CNT-based catalyst, showing features that could be of interest for further studies. Gasification of the AC support seems to be avoided in the case of the P-containing catalyst. In addition, the presence of mesopores, which can allocate higher coke amounts before being blocked, and Ni_xP species that promote hydrogenation reactions, seem to delay the coke deactivation mechanisms, explaining the superior stability of the nickel catalysts obtained using the H_3PO_4-activated carbon.

This novel approach points out that sustainable hydrogen production can be attained by using agricultural waste both as feedstock for the pyrolysis process and as raw material to produce renewable carbon-based nickel catalysts with improved catalytic performance in the steam reforming of bio-oil.

Author statement

During the preparation of this work the authors not used AI-assisted technologies in the writing process.

CRediT authorship contribution statement

Paula Cabrera-Reyes: Conceptualization, Formal analysis, Investigation, Methodology, Writing – original draft. **José Palomo:** Data curation, Formal analysis, Methodology, Writing – original draft. **Francisco J. García-Mateos:** Data curation, Formal analysis, Validation. **Ramiro Ruiz-Rosas:** Conceptualization, Data curation, Supervision, Validation, Visualization, Writing – review & editing. **Juana M. Rosas:** Conceptualization, Project administration, Resources, Supervision, Writing – review & editing, Funding acquisition. **José Rodríguez-Mirasol:** Project administration, Resources, Validation, Writing – review & editing, Funding acquisition. **Tomás Cordero:** Funding acquisition, Resources, Visualization.

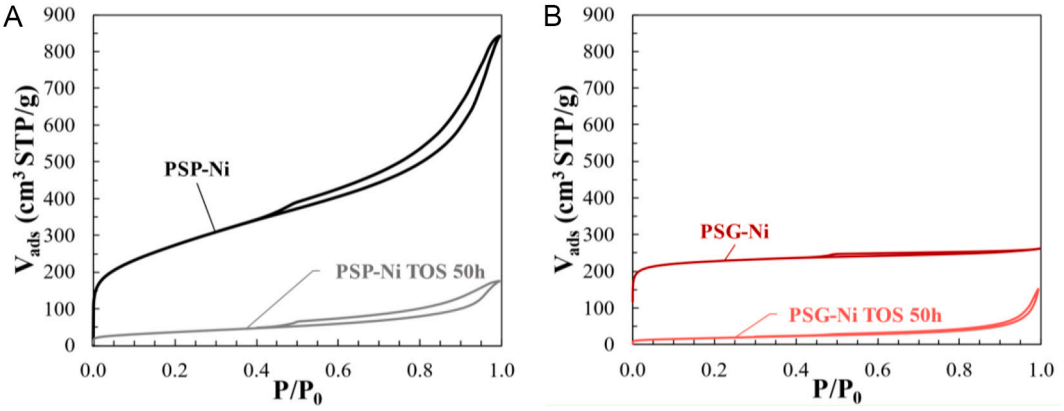

Fig. 12. N_2 adsorption-desorption isotherms at −196 °C of A) PSP-Ni and B) PSG-Ni fresh and used catalysts (TOS: 50 h).

Declaration of Competing Interest

The authors declare that they have no known competing financial interests or personal relationships that could have appeared to influence the work reported in this paper.

Data availability

Data will be made available on request.

Acknowledgements

This work was supported by MCIN (PID2022-140844OB-I00) and MCIN and European Union "NextGenerationEU"/PRTR (MCIN/AEI/10.13039/501100011033) and (TED2021-131324B-C21). Funding for open access charge: Universidad de Málaga / CBUA. P.C-R gratefully acknowledges University of Malaga for the support through a predoctoral grant.

Appendix A. Supplementary data

Supplementary data to this article can be found online at https://doi.org/10.1016/j.fuproc.2023.108028.

References

[1] Statistical Review of World Energy, Energy Economics | Home, last accessed: 2023/12/06, https://www.bp.com/en/global/corporate/energy-economics/statistical-review-of-world-energy.html, 2023.
[2] Communication from the Commission to the European Parliament, the Council, the European Economic and Social Committee and the Committee of the Regions, A hydrogen Strategy for a Climate-Neutral Europe, European Comission, 2020 last accessed: 2022/09/12, https://eur-lex.europa.eu/legal-content/EN/TXT/?uri=CELEX%3A52020DC0301.
[3] P. Nikolaidis, A. Poullikkas, Renew. Sust. Energ. Rev. 67 (2017) 597–611.
[4] M.C. Gutiérrez, J.M. Rosas, M.A. Rodríguez-Cano, I. López-Luque, J. Rodríguez-Mirasol, T. Cordero, Energy Convers. Manag. 182 (2019) 201–214.
[5] F. Wang, D. Ouyang, Z. Zhou, S.J. Page, D. Liu, X. Zhao, J. Energy Chem. 57 (2021) 247–280.
[6] G.H. Delmas, J.H. Banoub, M. Delmas, Waste and Biomass Valorization, 2021 13:5 13, 2021, pp. 2477–2491.
[7] P. Tarifa, N. Schiaroli, P.H. Ho, F. Cañaza, F. Ospitali, G. Sanghez de Luna, C. Lucarelli, G. Fornasari, A. Vaccari, A. Monzon, P. Benito, Catal. Today 383 (2022) 74–83.
[8] M. González-castaño, E. Le Saché, C. Berry, L. Pastor-pérez, H. Arellano-garcía, Q. Wang, T.R. Reina, Catalysts 11 (2021) 446, 2021, Vol. 11, Page 446.
[9] B. Hu, Z. Xi Zhang, W. Luan Xie, J. Liu, Y. Li, W. Ming Zhang, H. Fu, Q. Lu, Fuel Process. Technol. 237 (2022) 107465.
[10] F.G.E. Nogueira, P.G.M. Assaf, H.W.P. Carvalho, E.M. Assaf, Appl. Catal. B 160–161 (2014) 188–199.
[11] A.V. Bridgwater, Biomass Bioenergy 38 (2012) 68–94.
[12] X. Hu, M. Gholizadeh, J. Energy Chem. 39 (2019) 109–143.
[13] C. Rioche, S. Kulkarni, F.C. Meunier, J.P. Breen, R. Burch, Appl. Catal. B 61 (2005) 130–139.
[14] L. Garcia, R. French, S. Czernik, E. Chornet, Appl. Catal. A Gen. 201 (2000) 225–239.
[15] D. Li, X. Li, J. Gong, Chem. Rev. 116 (2016) 11529–11653.
[16] F. Bimbela, D. Chen, J. Ruiz, L. García, J. Arauzo, Appl. Catal. B 119–120 (2012) 1–12.
[17] A.C. Basagiannis, X.E. Verykios, Appl. Catal. A Gen. 308 (2006) 182–193.
[18] F. Seyedeyn Azad, J. Abedi, E. Salehi, T. Harding, Chem. Eng. J. 180 (2012) 145–150.
[19] R.S. Tan, T.A. Tuan Abdullah, S.A. Mahmud, R. Md Zin, K. Md Isa, Int. J. Hydrog. Energy 44 (2019) 21303–21314.
[20] E. Salehi, F.S. Azad, T. Harding, J. Abedi, Fuel Process. Technol. 92 (2011) 2203–2210.
[21] L. Landa, J. Valecillos, A. Remiro, B. Valle, J. Bilbao, A.G. Gayubo, Chem. Eng. J. 458 (2023) 141494.
[22] B. Beguin, E. Garbowski, M. Primet, J. Catal. 127 (1991) 595–604.
[23] F. Bimbela, M. Oliva, J. Ruiz, L. García, J. Arauzo, J. Anal. Appl. Pyrolysis 79 (2007) 112–120.
[24] J. Chen, J. Sun, Y. Wang, Ind. Eng. Chem. Res. 56 (2017) 4627–4637.
[25] K. Gao, M.C. Iliuta, J. Energy Chem. 73 (2022) 485–512.
[26] T. Furusawa, K. Saito, Y. Kori, Y. Miura, M. Sato, N. Suzuki, Fuel 103 (2013) 111–121.
[27] L. He, S. Hu, L. Jiang, G. Liao, X. Chen, H. Han, L. Xiao, Q. Ren, Y. Wang, S. Su, J. Xiang, Fuel Process. Technol. 176 (2018) 7–14.
[28] P. Serp, J.L. Figueiredo, Carbon Materials for Catalysis, 2008, pp. 1–579.
[29] J. Palomo, J.J. Ternero-Hidalgo, J.M. Rosas, J. Rodríguez-Mirasol, T. Cordero, Fuel Process. Technol. 156 (2017) 438–445.
[30] T.J. Bandosz, C.O. Ania, Interface Sci. Technol. 7 (2006) 159–229.
[31] M.J. Valero-Romero, F.J. García-Mateos, J. Rodríguez-Mirasol, T. Cordero, Fuel Process. Technol. 157 (2017) 116–126.
[32] J.M. Rosas, R. Ruiz-Rosas, J. Rodríguez-Mirasol, T. Cordero, Carbon 50 (2012) 1523–1537.
[33] D. Buentello-Montoya, X. Zhang, J. Li, V. Ranade, S. Marques, M. Geron, Appl. Energy 259 (2020) 114176.
[34] K. Qian, A. Kumar, Fuel 187 (2017) 128–136.
[35] C. Di Stasi, M. Cortese, G. Greco, S. Renda, B. González, V. Palma, J.J. Manyà, Int. J. Hydrog. Energy 46 (2021) 26915–26929.
[36] H.S.M. Yahya, T. Abbas, N.A.S. Amin, Int. J. Hydrog. Energy 46 (2021) 24632–24651.
[37] S. Li, J. Gong, Chem. Soc. Rev. 43 (2014) 7245–7256.
[38] N. Gao, J. Salisu, C. Quan, P. Williams, Renew. Sust. Energ. Rev. 145 (2021) 111023.
[39] M. Musso, A. Cardozo, M. Romero, R. Faccio, D. Segobia, C. Apesteguía, J. Bussi, Catal. Today 394–396 (2022) 524–538.
[40] G. Lu, Y. Bai, L. Ren, J. Wang, X. Song, G. Yu, Energy Convers. Manag. 225 (2020) 113471.
[41] X. Wang, Y. Liu, K. Liu, J. Zhang, J. Wei, Int. J. Hydrog. Energy 45 (2020) 28325–28336.
[42] J.M. Rosas, J. Bedia, J. Rodríguez-Mirasol, T. Cordero, Fuel 88 (2009) 19–26.
[43] J. Bedia, R. Ruiz-Rosas, J. Rodríguez-Mirasol, T. Cordero, J. Catal. 271 (2010) 33–42.
[44] J.M. Rosas, R. Ruiz-Rosas, J. Rodríguez-Mirasol, T. Cordero, Carbon 50 (2012) 1523–1537.
[45] J.M. Rosas, R. Ruiz-Rosas, J. Rodríguez-Mirasol, T. Cordero, Catal. Today 187 (2012).
[46] I. Hita, T. Cordero-Lanzac, F.J. García-Mateos, M.J. Azkoiti, J. Rodríguez-Mirasol, T. Cordero, J. Bilbao, Appl. Catal. B 259 (2019) 118112.
[47] T. Cordero-Lanzac, R. Palos, J.M. Arandes, P. Castaño, J. Rodríguez-Mirasol, T. Cordero, J. Bilbao, Appl. Catal. B 203 (2017) 389–399.
[48] B. Hosseinzaei, M.J. Hadianfard, R. Ruiz-Rosas, J.M. Rosas, J. Rodríguez-Mirasol, T. Cordero, J. Anal. Appl. Pyrolysis 168 (2022) 105724.
[49] M. Thommes, K. Kaneko, A.V. Neimark, J.P. Olivier, F. Rodriguez-Reinoso, J. Rouquerol, K.S.W. Sing, Pure Appl. Chem. 87 (2015) 1051–1069.
[50] J.A. Cecilia, A. Infantes-Molina, E. Rodríguez-Castellón, A. Jiménez-López, J. Catal. 263 (2009) 4–15.
[51] I. Czekaj, F. Loviat, F. Raimondi, J. Wambach, S. Biollaz, A. Wokaun, Appl. Catal. A Gen. 329 (2007) 68–78.
[52] A.P. Grosvenor, M.C. Biesinger, R.S.C. Smart, N.S. McIntyre, Surf. Sci. 600 (2006) 1771–1779.
[53] D. Yang, Q. Yu, L. Gao, L. Mao, J.H. Yang, Appl. Surf. Sci. 416 (2017) 503–510.
[54] A. Wang, M. Qin, J. Guan, L. Wang, H. Guo, X. Li, Y. Wang, R. Prins, Y. Hu, Angew. Chem. Int. Ed. 47 (2008) 6052–6054.
[55] M.J. Valero-Romero, E.M. Calvo-Muñoz, R. Ruiz-Rosas, J. Rodríguez-Mirasol, T. Cordero, Ind. Eng. Chem. Res. 58 (2019) 4042–4053.
[56] X. Guo, A. Traitangwong, M. Hu, C. Zuo, V. Meeyoo, Z. Peng, C. Li, Energy Fuel 32 (2018) 3681–3689.
[57] C.H. Bartholomew, Catal. Rev. 24 (1982) 67–112.
[58] B. Hosseinzaei, M.J. Hadianfard, B. Aghabarari, M. García-Rollán, R. Ruiz-Rosas, J. M. Rosas, J. Rodríguez-Mirasol, T. Cordero, Bioresour. Technol. Rep. 19 (2022) 101209.
[59] H. Yang, P. de Wild, C.W. Lahive, Z. Wang, P.J. Deuss, H.J. Heeres, Fuel Process. Technol. 228 (2022) 107160.
[60] J.A. Medrano, M. Oliva, J. Ruiz, L. García, J. Arauzo, Energy 36 (2011) 2215–2224.
[61] H. Xie, Q. Yu, X. Yao, W. Duan, Z. Zuo, Q. Qin, J. Energy Chem. 24 (2015) 299–308.
[62] C. Hognon, C. Dupont, M. Grateau, F. Delrue, Bioresour. Technol. 164 (2014) 347–353.
[63] X. Hu, G. Lu, Appl. Catal. B 88 (2009) 376–385.
[64] G. Chen, J. Tao, C. Liu, B. Yan, W. Li, X. Li, Renew. Sust. Energ. Rev. 79 (2017) 1091–1098.
[65] S. Ogo, Y. Sekine, Fuel Process. Technol. 199 (2020) 106238.
[66] S.T. Oyama, T. Gott, H. Zhao, Y.K. Lee, Catal. Today 143 (2009) 94–107.
[67] N. Koike, S. Hosokai, A. Takagaki, S. Nishimura, R. Kikuchi, K. Ebitani, Y. Suzuki, S.T. Oyama, J. Catal. 333 (2016) 115–126.
[68] A.G. Gayubo, B. Valle, B. Aramburu, C. Montero, J. Bilbao, Chem. Eng. J. 332 (2018) 192–204.
[69] J. Chen, M. Wang, S. Wang, X. Li, Int. J. Hydrog. Energy 43 (2018) 18160–18168.
[70] S. Wang, F. Zhang, Q. Cai, X. Li, L. Zhu, Q. Wang, Z. Luo, Int. J. Hydrog. Energy 39 (2014) 2018–2025.
[71] F. Bimbela, M. Oliva, J. Ruiz, L. García, J. Arauzo, J. Anal. Appl. Pyrolysis 79 (2007) 112–120.
[72] A.C. Basagiannis, X.E. Verykios, Appl. Catal. A Gen. 308 (2006) 182–193.
[73] Z. Zhang, X. Hu, J. Li, G. Gao, D. Dong, R. Westerhof, S. Hu, J. Xiang, Y. Wang, Fuel 217 (2018) 389–403.
[74] A.N. Fatsikostas, D.I. Kondarides, X.E. Verykios, Catal. Today 75 (2002) 145–155.
[75] D.L. Trimm, Catal. Today 49 (1999) 3–10.
[76] I. Alstrup, N.T. Andersen, J. Catal. 104 (1987) 466–479.
[77] S.T. Oyama, J. Catal. 216 (2003) 343–352.
[78] J. Rostrup-Nielsen, D.L. Trimm, J. Catal. 48 (1977) 155–165.
[79] D.L. Trimm, Catal. Rev. 16 (1977) 155–189.

[80] M.A. Nieva, M.M. Villaverde, A. Monzón, T.F. Garetto, A.J. Marchi, Chem. Eng. J. 235 (2014) 158–166.
[81] F.M. Bkangmo Kontchouo, Y. Shao, S. Zhang, M. Gholizadeh, X. Hu, Chem. Eng. Sci. 265 (2023) 118257.
[82] F.J. García-Mateos, J.M. Rosas, R. Ruiz-Rosas, J. Rodríguez-Mirasol, T. Cordero, Carbon 200 (2022) 134–148.
[83] P. Lu, Q. Huang, A.C. Bourtsalas, Y. Chi, J. Yan, Waste Biomass Valoriz 10 (2019) 155–165.
[84] R.A. DiLeo, B.J. Landi, R.P. Raffaelle, J. Appl. Phys. 101 (2007) 064307.
[85] M.L. Toebes, J.H. Bitter, A. Jos Van Dillen, K.P. De Jong, Catal. Today 76 (2002) 33–42.
[86] S. Liu, Z. Yan, Y. Zhang, R. Wang, S.Z. Luo, F. Jing, W. Chu, ACS Sustain. Chem. Eng. 6 (2018) 14403–14413.
[87] C.H. Bartholomew, Appl. Catal. A Gen. 212 (2001) 17–60.
[88] D. Buentello-Montoya, X. Zhang, J. Li, V. Ranade, S. Marques, M. Geron, Appl. Energy 259 (2020) 114176.
[89] Q.H. Yang, P.X. Hou, S. Bai, M.Z. Wang, H.M. Cheng, Chem. Phys. Lett. 345 (2001) 18–24.